

In Situ Electrochemically Derived Nanoporous Oxides from Transition Metal Dichalcogenides for Active Oxygen Evolution Catalysts

Wei Chen,[†] Yayuan Liu,[†] Yuzhang Li,[†] Jie Sun,[†] Yongcai Qiu,[†] Chong Liu,[†] Guangmin Zhou,[†] and Yi Cui^{*,†,‡}

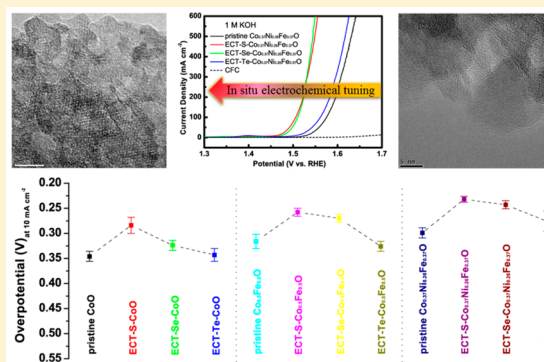
[†]Department of Materials Science and Engineering, Stanford University, Stanford, California 94305, United States

[‡]Stanford Institute for Materials and Energy Sciences, SLAC National Accelerator Laboratory, Menlo Park, California 94025, United States

S Supporting Information

ABSTRACT: Transition metal dichalcogenides have been widely studied as active electrocatalysts for hydrogen evolution reactions. However, their properties as oxygen evolution reaction catalysts have not been fully explored. In this study, we systematically investigate a family of transition metal dichalcogenides (MX, M = Co, Ni, Fe; X = S, Se, Te) as candidates for water oxidation. It reveals that the transition metal dichalcogenides are easily oxidized in strong alkaline media via an in situ electrochemical oxidation process, producing nanoporous transition metal oxides toward much enhanced water oxidation activity due to their increased surface area and more exposed electroactive sites. The optimal cobalt nickel iron oxides that derived from their sulfides and selenides demonstrate a low overpotential of 232 mV at current density of 10 mA cm⁻², a small Tafel slope of 35 mV per decade, and negligible degradation of electrochemical activity over 200 h of electrolysis. This study represents the discovery of nanoporous transition metal oxides deriving from their chalcogenides as outstanding electrocatalysts for water oxidation.

KEYWORDS: *in situ electrochemical tuning, transition metal chalcogenides, nanoporous metal oxides, oxygen evolution reaction, electrocatalysts*



Water oxidation catalysts (WOCs) have been attracting significant attention owing to their promising applications in green and sustainable energy storage and conversion schemes with connection to fuel cells, metal air batteries, and solar water splitting devices.^{1–5} They also play important roles in biological systems where the water oxidation reactions take place in the oxygen evolving complex of photosystem II in plants.^{6–8} However, the development of highly active WOCs is very challenging due to the high thermodynamic potential required for water oxidation (1.23 V vs NHE at pH 0) and the sluggish kinetic hindrance of the multielectron-evolving charge-transfer reactions.^{9–11} Transition metal oxides (TMOs) and their derivatives (hydroxides, oxyhydroxides, etc.) are the most investigated WOCs with a high activity and stability.^{12,13} Although the state-of-the-art precious transition metal based WOCs such as IrO₂ and RuO₂ show great activities toward oxygen evolution reactions (OER), the scarcity of the precious metals on earth and their prohibitively high costs impede their commercial large-scale applications.¹⁴ Therefore, low cost earth-abundant TMOs are emerging as an important category of WOCs that were explored extensively by researchers. It was reported that porous TMOs showed higher OER activity than

that of their nonporous counterparts due to the increased surface area and more exposed electroactive sites.^{15–17} Nanomaterials afford great possibilities to design a wide range of TMOs with large surface areas. For example, mesoporous Co₃O₄ with an open framework structure and a high surface area showed enhanced OER activity compared to that of the bulk Co₃O₄.¹⁸ A nanoporous nickel cobalt binary oxide film showed a low overpotential of 325 mV at a current density of 10 mA cm⁻² and a small Tafel slope of 39 mV dec⁻¹.¹⁹

Transition metal dichalcogenides (denoted as MXs; where M represents a transition metal such as Fe, Co, Ni, Mo, W, etc. and X represents the chalcogen of S, Se, and Te) are emerging as excellent materials in different applications such as transistors, superconductors, batteries, solar cells, and catalysis, owing to their unique physical and chemical properties.^{20–38} Particularly, MXs are heavily employed as hydrogen evolution reaction catalysts.^{39–44} However, their properties as WOCs

Received: August 16, 2016

Revised: November 14, 2016

Published: November 28, 2016

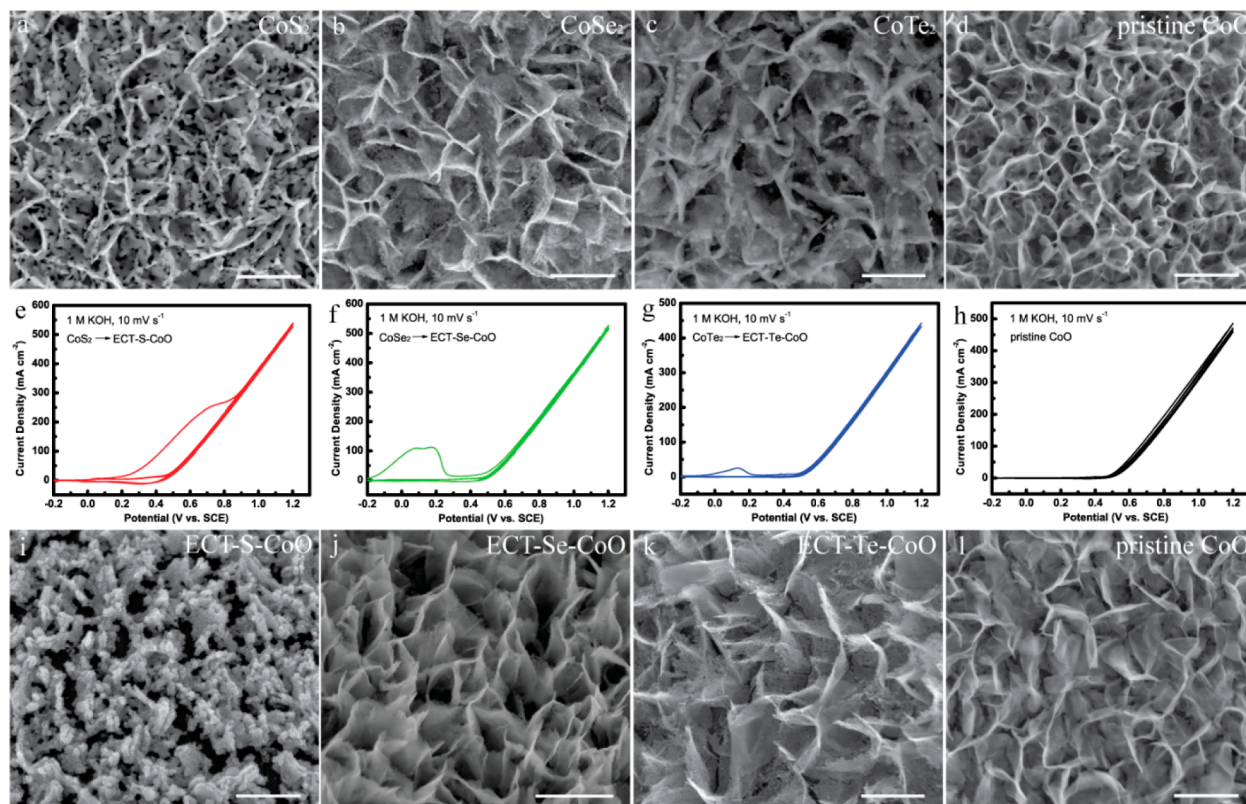


Figure 1. In situ electrochemical oxidation tuning process of cobalt dichalcogenides. SEM images of (a) CoS_2 , (b) CoSe_2 , (c) CoTe_2 , and (d) pristine CoO before tuning. The electrochemical tuning processes of (e) CoS_2 , (f) CoSe_2 , (g) CoTe_2 , and (h) the pristine CoO in 1 M KOH electrolyte at the same scan rate of 10 mV s^{-1} , respectively. The CV curves contain three consecutive oxidation–reduction scans. SEM images of (i) CoS_2 , (j) CoSe_2 , (k) CoTe_2 , and (l) pristine CoO after the electrochemical tuning. Scale bars: 500 nm.

have not been thoroughly investigated. A few studies have been reported that some MXs such as Co_3S_4 , Ni_3S_2 , NiCo_2S_4 , and CoSe_2 exhibited excellent OER activity as WOCs.^{45–50} However, it has been recently found that the MXs such as NiSe are highly likely to be oxidized to form a surface layer of NiOOH serving as active sites for water oxidation.⁵¹ We have recently demonstrated that transition metal sulfides are easily oxidized by a so-called in situ electrochemical oxidation tuning methodology to form nanoporous transition metal oxides for enhanced water oxidation.⁵² Nevertheless, it is still ambiguous whether the other MXs such as selenides and tellurides can also be in situ tuned to TMOs. If yes, what is the impact of the in situ electrochemical tuning on the morphology, structure, and OER performance of the chalcogenides derived TMOs? To answer these questions and to further explore active WOCs, we adopt in this study the in situ electrochemical oxidation tuning method to develop a whole family of MXs including sulfides, selenides, and tellurides to systematically investigate their properties as OER catalysts. It is revealed that the MXs are easily to be oxidized by the in situ electrochemical tuning, generating nanoporous metal oxides (oxyhydroxides) with high surface areas. The dichalcogenides derived nanoporous oxides exhibit excellent electrocatalytic performance for water oxidation.

The family of nanoporous transition metal (e.g., Co , Ni , and Fe) oxides with a controllable metal composition was successfully derived from their corresponding chalcogenides by the in situ electrochemical oxidation tuning process. The fabrication of the MXs involves the electrodeposition of pristine metal oxides and the subsequent sulfurization/selenization/

tellurization treatments at high temperature in order to produce the corresponding metal sulfides/selenides/tellurides (see [Experimental Section](#) for details). Taking the binary CoO as an example, the cobalt chalcogenides (CoX) including CoS_2 (Figure 1a), CoSe_2 (Figure 1b), and CoTe_2 (Figure 1c) were produced from the pristine CoO (Figure 1d). Subsequently, the facile in situ electrochemical oxidation tuning process enables the formation of the chalcogenide derived CoO (referred to as ECT-X- CoO ; where X stands for the specific chalcogenides of S, Se, or Te that the CoO was derived from). The whole process can be denoted as pristine- $\text{CoO}/\text{CoX}/\text{ECT-X-}\text{CoO}$. As shown in Figure 1a–d, the CoX maintain the overall nanosheet morphology of the pristine CoO that were grown directly on the conductive carbon fiber substrates (Figure 1d, Figure S1). However, the obtained CoS_2 (Figure 1a), CoSe_2 (Figure 1b), and CoTe_2 (Figure 1c) exhibit porous nanostructures due to their high-temperature sulfurization/selenization/tellurization treatments, drastically different from the smooth surface of the pristine CoO nanosheets (Figure 1d). The electrochemical behaviors of the CoS_2 , CoSe_2 , and CoTe_2 by the in situ electrochemical oxidation tuning are shown in Figure 1e, f, and g, respectively. Different from the highly repeated cyclic voltammetry (CV) behaviors of the pristine CoO (Figure 1h), it was found that an irreversible oxidation peak appears in CV curves of all CoX . The pronounced oxidation peaks appear where the chalcogenides are transformed to oxides. However, the distinct irreversible oxidation peaks disappear completely in the following CV scans, indicating that the chalcogenides are fully transformed to oxides in the very first oxidation process. It is also noticed that the intensity of the oxidation peaks of CoX

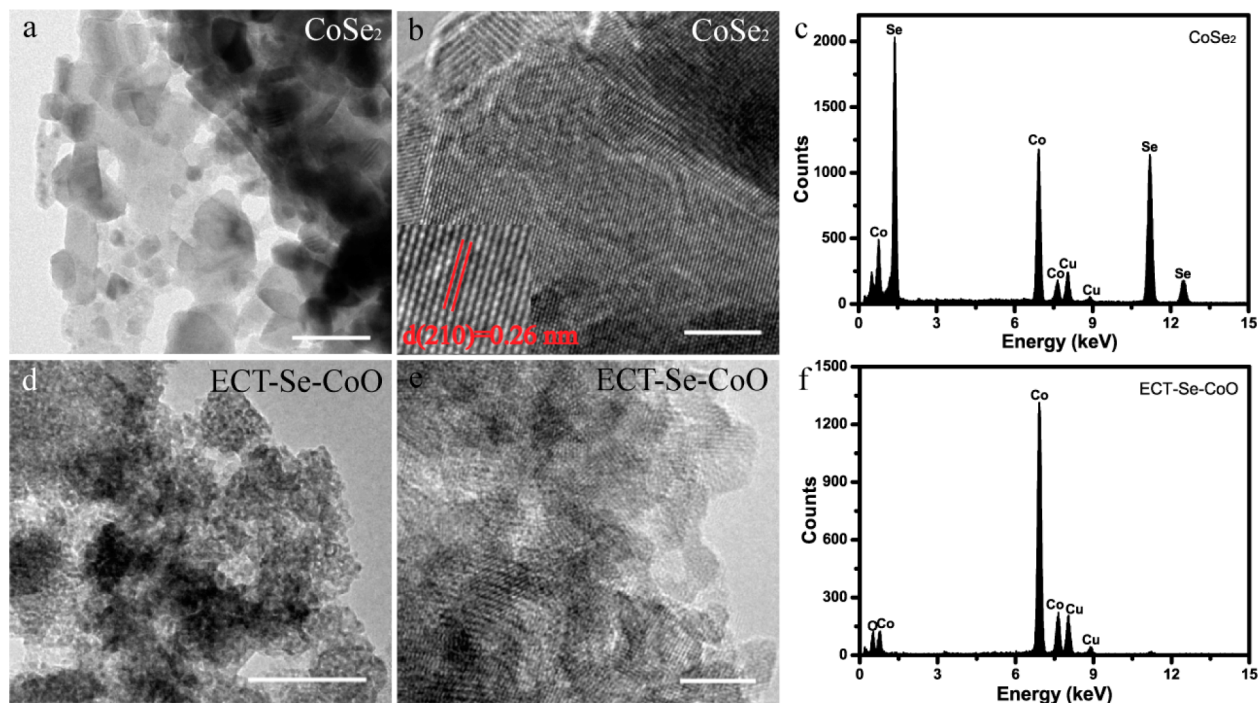


Figure 2. TEM characterization of CoSe_2 and ECT-Se-CoO. (a) TEM, (b) HRTEM, and (c) EDX of CoSe_2 , respectively. (d) TEM, (e) HRTEM, and (f) EDX of ECT-Se-CoO, respectively. Scale bars: (a, d) 50 nm; (b, e) 5 nm.

decreases in the order of CoS_2 , CoSe_2 , and CoTe_2 under the same scan rate of 10 mV s^{-1} , which is probably due to the decreased oxidation activity and kinetics of the chalcogenides with respect to the alkaline solution (Figure S2). Figure 1i–l shows the morphology of the resulting ECT-X-CoO after the in situ electrochemical oxidation tuning. It is observed that the ECT-S-CoO has drastically different morphology from the CoS_2 , where the porous CoS_2 nanosheets with large crystal grains have broken into smaller grains that are interconnected with each other, thereby creating numerous nanopores on the ECT-S-CoO. The ECT-Se/Te-CoO inherits the nanosheet morphology of their CoSe_2 and CoTe_2 , while a significant amount of nanopores were also introduced into the ECT-Se/Te-CoO as will be revealed in the following contents. In contrast, the in situ electrochemical tuning has little effect to the pristine CoO , where their morphology kept the same as original ones (Figure 1l).

Looking into the detailed morphology and composition evolution of the pristine-CoO/ CoX /ECT-X-CoO process, one can observe from transmission electron microscopy (TEM) image that the CoX (CoSe_2 as an example) shows porous nanosheets with numerous mesopores generated by the high temperature selenization treatment due to the displacement of oxygen atoms by selenium atoms and the crystal growth of CoSe_2 (Figure 2a). The crystal grain size of the CoSe_2 is as large as tens of nanometers as shown in Figure 2b. However, the ECT-Se-CoO after the in situ electrochemical oxidation tuning of CoSe_2 in 1 M KOH exhibits even more porous nanostructures, in which some bigger mesopores and numerous smaller nanoporous are clearly visible (Figure 2d). It is further demonstrated in HRTEM that the nanopores are typically with size less than 5 nm (Figure 2e). The X-ray energy dispersive spectroscopy (EDX) of CoSe_2 shows the coexistence of both Co and Se elements (Figure 2c). However, the intensive Se peaks disappear completely in the ECT-Se-CoO,

confirming the successful transformation of CoSe_2 to ECT-Se-CoO that induced by the electrochemical oxidation tuning (Figure 2f). As for the systems of CoS_2 /ECT-S-CoO and CoTe_2 /ECT-Te-CoO, we have also observed the similar morphology and crystal evolution as a result of the in situ electrochemical oxidation tuning (Figure S3). These observations indicate that the in situ electrochemical oxidation tuning approach has a great impact on tuning the crystal structure, grain size, porosity, and surface area of the MXs.

X-ray diffraction (XRD) and X-ray photoelectron spectroscopy (XPS) were further performed to reveal the electrochemical tuning on ECT-X-CoO. As shown in Figure 3a, the electrochemical tuning has little effect on the crystal structure of the pristine CoO , which shows almost the same characteristic peaks after tuning. In comparison, the electrochemical tuning exhibits significant alternations on the crystal structure of CoX_2 , where CoSe_2 , CoS_2 , and CoTe_2 changed from highly crystalline to nearly amorphous structures (Figure 3a, Figure S4). It is well-known that there are two basic crystal structures in the metal dichalcogenides: the cubic pyrite type (Figure 3b) and the orthorhombic marcasite type (Figure 3c).^{37,43,53} In both types of structures, the metal atoms are bonded to adjacent chalcogen atoms octahedrally. They can be distinguished by the octahedral linkage, where the pyrite type shows corner-shared and the marcasite type shows edge-shared octahedral, respectively.⁴³ In the case of CoSe_2 , it is demonstrated in Figure 3a that the majority of characteristic peaks correspond to the cubic pyrite phase of CoSe_2 (PDF no. 04-003-1990), together with a few weak peaks that are ascribed to the marcasite phase of CoSe_2 (PDF no. 00-053-0449). Such crystal structure behaviors of the CoSe_2 are widely observed in the literature and are very consistent with our previously reported CoSe_2 , where the marcasite phase is tend to grow epitaxially on the pyrite phase due to their similar structures but small lattice mismatch between the two phases.^{43,54–56} The

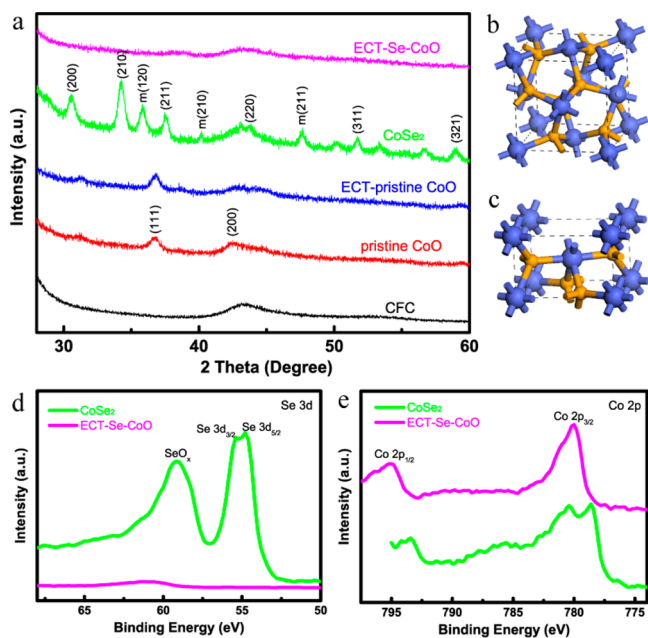


Figure 3. XRD and XPS characterization of CoSe_2 and ECT-Se-CoO. (a) XRD of CFC, pristine CoO, ECT-pristine CoO, CoSe_2 , and ECT-Se-CoO. Schematic crystal structures of CoSe_2 in (b) cubic pyrite type and (c) orthorhombic marcasite type phases, respectively. (d) Se 3d and (e) Co 2p core-level XPS spectra of CoSe_2 and ECT-Se-CoO.

XPS spectra of the CoSe_2 shows the coexistence of Co and Se (Figure 3d,e), confirming the successful preparation of the CoSe_2 which is consistent with the observation by EDX (Figure 2c). The peaks of Se $3d_{3/2}$ around 55.4 eV and Se $3d_{5/2}$ around 54.8 eV are in good agreement with Se_2^{2-} in CoSe_2 , whereas the peak at binding energy of 59.2 eV corresponds to SeO_x .^{43,57} It is found that the Se 3d peaks disappear completely in ECT-Se-CoO, indicating that the CoSe_2 is completely converted to ECT-Se-CoO (Figure 3d). However, there exists a small fraction of SeO_x traces probably because of those inactivated portions in response to OH^- . It is further revealed that the SeO_x peak has been shifted to higher binding energy, demonstrating that the very small portion of Se residues in ECT-Se-CoO have been oxidized to higher oxidation state when not fully oxidized. The electron binding energies of Co $2p_{1/2}$ at 793.5 eV and Co $2p_{3/2}$ at 778.6 eV in CoSe_2 correspond to Co^{2+} species.^{57,58} The shakeup satellite around 780.4 eV at higher energy side of Co $2p_{3/2}$ in CoSe_2 is a result of the antibonding orbital between the Co and Se atoms.^{57,58} This behavior has been observed and recognized in the previous studies on CoSe_2 .^{59,60} However, the Co 2p peaks in ECT-Se-CoO have been shifted to higher binding energies after the electrochemical oxidation tuning (Figure 3e). The binding energies of Co $2p_{1/2}$ at 795.2 eV and Co $2p_{3/2}$ at 780.1 eV in ECT-Se-CoO correspond to Co^{3+} , which were also observed in the ECT-S-CoO and ECT-Te-CoO (Figure S5).⁶¹ The ECT-X-CoO was further identified to be CoOOH , which agrees well with reported studies.⁶² It was reported that higher oxidation states in WOCs can help driving better electrocatalytic activities toward water oxidation.⁶³ These results indicate that the in situ electrochemical oxidation tuning enables the oxidation of both transition metals and chalcogens, showing the capability of the electrochemical oxidation tuning to different elements and materials.

Apart from the binary CoO, the electrochemical oxidation tuning methodology is highly applicable to generate a whole family of TMOs with different compositions, including ternary ECT-X- $\text{Co}_{0.5}\text{Fe}_{0.5}\text{O}$ and quaternary ECT-X- $\text{Co}_{0.37}\text{Ni}_{0.26}\text{Fe}_{0.37}\text{O}$ that derived from different transition metal chalcogenides. As shown in Figure S6 and S7, the ECT-X- $\text{Co}_{0.5}\text{Fe}_{0.5}\text{O}$ and ECT-X- $\text{Co}_{0.37}\text{Ni}_{0.26}\text{Fe}_{0.37}\text{O}$ exhibit the similar morphology evolution as to that of the ECT-X-CoO, highlighting the versatility of the in situ electrochemical oxidation tuning to different materials. For example, the quaternary $\text{Co}_{0.37}\text{Ni}_{0.26}\text{Fe}_{0.37}\text{Se}_2$ displays morphology of porous nanosheets which consist of many individual nanoparticles that are interlinked with each other (Figure 4a). The $\text{Co}_{0.37}\text{Ni}_{0.26}\text{Fe}_{0.37}\text{Se}_2$ nanoparticles with typical size larger than 10 nm show highly crystalline characteristic, as depicted by the crystalline fringes of their (210) plane in Figure 4b. In contrast, the ECT-Se- $\text{Co}_{0.37}\text{Ni}_{0.26}\text{Fe}_{0.37}\text{O}$ demonstrates entirely different morphology and crystalline features. Specifically, the relatively large nanoparticles of $\text{Co}_{0.37}\text{Ni}_{0.26}\text{Fe}_{0.37}\text{Se}_2$ were broken into numerous tiny nanoparticles by creating a significant amount of nanopores, grain boundaries and defects, thus making the ECT-Se- $\text{Co}_{0.37}\text{Ni}_{0.26}\text{Fe}_{0.37}\text{O}$ nanosheets highly porous (Figure 4c). It is further revealed by HRTEM image that these tiny ECT-Se- $\text{Co}_{0.37}\text{Ni}_{0.26}\text{Fe}_{0.37}\text{O}$ nanoparticles are mostly less than 5 nm (Figure 4d). In the meanwhile, they show very weak crystallinity that is totally distinguished from the highly crystalline $\text{Co}_{0.37}\text{Ni}_{0.26}\text{Fe}_{0.37}\text{Se}_2$ nanocrystals. Furthermore, a similar materials evolution was also observed in the systems of $\text{Co}_{0.37}\text{Ni}_{0.26}\text{Fe}_{0.37}\text{S}_2$ /ECT-S- $\text{Co}_{0.37}\text{Ni}_{0.26}\text{Fe}_{0.37}\text{O}$ and $\text{Co}_{0.37}\text{Ni}_{0.26}\text{Fe}_{0.37}\text{Te}_2$ /ECT-Te- $\text{Co}_{0.37}\text{Ni}_{0.26}\text{Fe}_{0.37}\text{O}$ (Figure S8), confirming the versatility of the in situ electrochemical oxidation tuning approach (Figure S9).

The OER activity of the catalysts was thoroughly investigated in 1 M KOH electrolyte by different catalytic techniques. Conductive carbon fiber cloth (CFC) was chosen as the substrate for the integrated 3D electrodes due to its negligible OER activity within the studied voltage ranges. Figure 5a shows the OER polarization curves of the nanoporous ECT-X-CoO and the pristine CoO. As compared to the pristine CoO, the ECT-S-CoO and ECT-Se-CoO exhibit much higher currents and lower onset potentials, indicating their better OER activities. However, the ECT-Te-CoO exhibits only slightly better performance than that of the pristine CoO at low current density. The Tafel plots of the ECT-X-CoO (Figure 5b) display slightly smaller slopes than that of the pristine CoO, suggesting the improved catalytic kinetics of the ECT-X-CoO. According to the polarization curves, it is evident that the ternary ECT-X- $\text{Co}_{0.5}\text{Fe}_{0.5}\text{O}$ (Figure S10) and quaternary ECT-X- $\text{Co}_{0.37}\text{Ni}_{0.26}\text{Fe}_{0.37}\text{O}$ (Figure 5c,d) systems also exhibit excellent OER activities with significant enhancement of OER activities than their pristine counterparts. The overpotentials of the pristine and ECT-X-TMOs are summarized in Figure 5e. It is found that the enhancement of OER activity of the TMOs via decreasing the onset overpotential can be achieved by two pathways: (1) the incorporation of Ni and Fe into CoO to form complex oxides, and (2) the in situ electrochemical oxidation tuning. We achieved greatly enhanced OER activity of TMOs by applying both approaches simultaneously. It is clearly shown in Figure 5e that the overpotentials of ternary $\text{Co}_{0.5}\text{Fe}_{0.5}\text{O}$ and quaternary $\text{Co}_{0.37}\text{Ni}_{0.26}\text{Fe}_{0.37}\text{O}$ at current density of 10 mA cm^{-2} are lower than the CoO, where the quaternary $\text{Co}_{0.37}\text{Ni}_{0.26}\text{Fe}_{0.37}\text{O}$ shows the lowest one. For example the overpotentials of the pristine TMOs are in the order of pristine CoO (346 mV) > pristine $\text{Co}_{0.5}\text{Fe}_{0.5}\text{O}$ (316 mV) > pristine

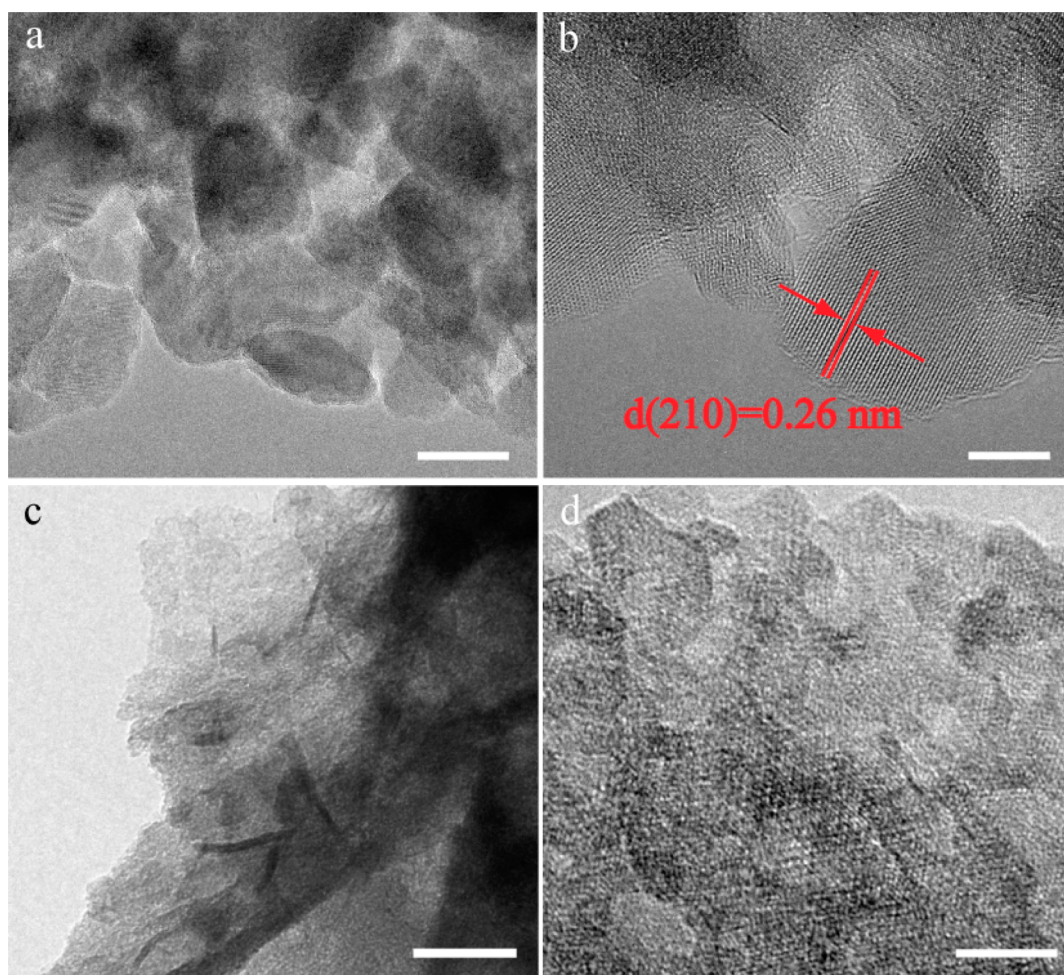


Figure 4. TEM and HRTEM images of the quaternary $\text{Co}_{0.37}\text{Ni}_{0.26}\text{Fe}_{0.37}\text{Se}_2$ and ECT-Se- $\text{Co}_{0.37}\text{Ni}_{0.26}\text{Fe}_{0.37}\text{O}$. (a, b) $\text{Co}_{0.37}\text{Ni}_{0.26}\text{Fe}_{0.37}\text{Se}_2$. (c, d) ECT-Se- $\text{Co}_{0.37}\text{Ni}_{0.26}\text{Fe}_{0.37}\text{O}$. Scale bars: (a) 20 nm; (c) 50 nm; (b, d) 5 nm.

$\text{Co}_{0.37}\text{Ni}_{0.26}\text{Fe}_{0.37}\text{O}$ (299 mV). As to the ECT-Se-TMOs, the order is ECT-Se-CoO (324 mV) > ECT-Se- $\text{Co}_{0.5}\text{Fe}_{0.5}\text{O}$ (270 mV) > ECT-Se- $\text{Co}_{0.37}\text{Ni}_{0.26}\text{Fe}_{0.37}\text{O}$ (243 mV) (Table S1). However, the enhancement of the OER activity by forming the complex oxides is limited by the intrinsic activity of different transition metals. Further significant improvement of OER activity was achieved by our in situ electrochemical oxidation tuning process, where the ECT-X-TMOs showed onset overpotentials much lower than that of the pristine TMOs (Figure 5e). For example, at a current density of 10 mA cm^{-2} , the overpotentials of the binary ECT-S-CoO (284 mV) and ECT-Se-CoO (324 mV) are much lower than that of the pristine CoO (346 mV), while the overpotentials of the quaternary ECT-S- $\text{Co}_{0.37}\text{Ni}_{0.26}\text{Fe}_{0.37}\text{O}$ (232 mV), ECT-Se- $\text{Co}_{0.37}\text{Ni}_{0.26}\text{Fe}_{0.37}\text{O}$ (243 mV), and ECT-Te- $\text{Co}_{0.37}\text{Ni}_{0.26}\text{Fe}_{0.37}\text{O}$ (276 mV) decreased by 67, 56, and 23 mV, respectively, as compared to the pristine $\text{Co}_{0.37}\text{Ni}_{0.26}\text{Fe}_{0.37}\text{O}$ (299 mV). Impressively, the onset overpotential of the ECT-S-CoO (284 mV) is even lower than that of the pristine $\text{Co}_{0.5}\text{Fe}_{0.5}\text{O}$ (316 mV) and $\text{Co}_{0.37}\text{Ni}_{0.26}\text{Fe}_{0.37}\text{O}$ (299 mV), indicating the great capabilities of the in situ electrochemical oxidation tuning approach. In terms of the Tafel slopes, it was summarized in Figure Sf that our TMOs have values in the range of 30–65 mV per decade, exhibiting relatively fast catalytic kinetics to drive a significant amount of water oxidation. The ECT-TMOs show generally lower Tafel slopes than that of the pristine ones.

Among them, the ternary ECT-S- $\text{Co}_{0.5}\text{Fe}_{0.5}\text{O}$ and ECT-Se- $\text{Co}_{0.5}\text{Fe}_{0.5}\text{O}$, as well as the quaternary ECT-S- $\text{Co}_{0.37}\text{Ni}_{0.26}\text{Fe}_{0.37}\text{O}$ and ECT-Se- $\text{Co}_{0.37}\text{Ni}_{0.26}\text{Fe}_{0.37}\text{O}$ showed optimal Tafel slopes of 38.9, 36.2, 37.6, and 35.1 mV dec^{-1} , respectively. The low onset overpotentials and small Tafel slopes of our ECT-TMOs are among the best values reported so far for nonprecious transition metal oxides and their derivatives as OER catalysts, as listed in Table S2.^{45,47–50,64}

The long-term electrolysis stability of the catalysts was evaluated by applying a constant current density of 20 mA cm^{-2} in 1 M KOH. As shown in Figures 6 and S11, the pristine TMOs show gradual increase of the overpotentials, indicating their gradual activity decay over long-term electrolysis. In contrast, the ECT-S-TMOs and ECT-Se-TMOs demonstrate exceptional durability with ultralong terms of water electrolysis, outperforming that of the pristine TMOs. Impressively, the ECT-S- $\text{Co}_{0.37}\text{Ni}_{0.26}\text{Fe}_{0.37}\text{O}$ and ECT-Se- $\text{Co}_{0.37}\text{Ni}_{0.26}\text{Fe}_{0.37}\text{O}$ exhibit a negligible increase of overpotential over 200 h, demonstrating their excellent stability for promising practical applications. It is identified that the ECT-Te-TMOs show decreased activity over a long-term test; however, their poor stability is not fully understood yet.

In order to elucidate the mechanism of the enhanced OER performance of the chalcogenides derived TMOs by in situ electrochemical oxidation tuning, we have carried out the surface area measurements by taking into account their

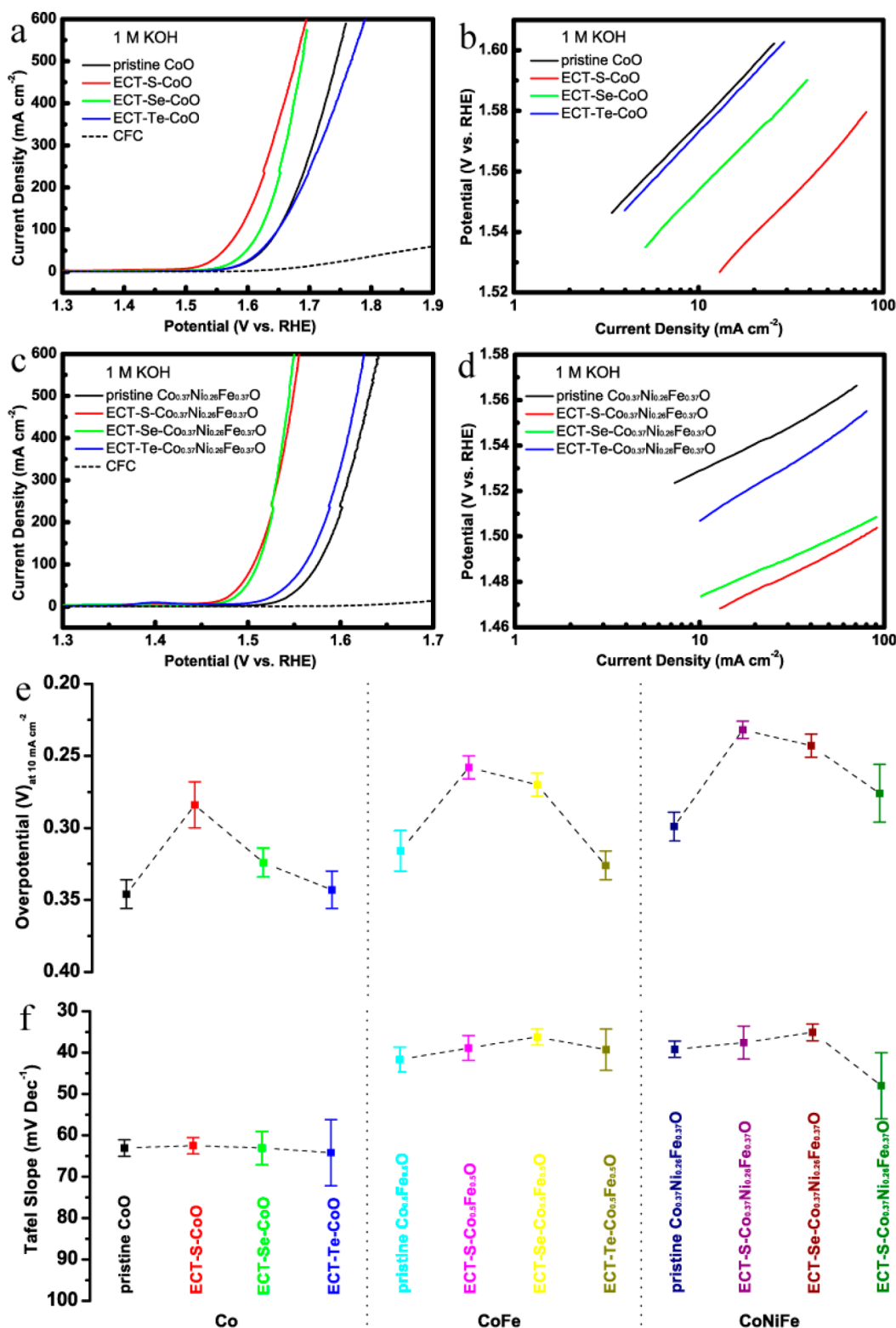


Figure 5. Electrocatalytic performance of the ECT-TMOs as compared to the pristine TMOs. (a) Polarization curves and (b) Tafel plots of the binary pristine CoO and ECT-X-CoO, respectively. (c) Polarization curves and (d) Tafel plots of the quaternary pristine Co_{0.37}Ni_{0.26}Fe_{0.37}O and ECT-X-Co_{0.37}Ni_{0.26}Fe_{0.37}O, respectively. Summary of (e) the overpotential at 10 mA cm⁻² and (f) the Tafel slope of the pristine TMOs and ECT-X-TMOs, respectively.

electrochemical double layer capacitance (EDLC). Figures S12 and S13 depict the EDLC measurement of the pristine CoO and ECT-X-CoO. The rectangular shapes of the CV curves over different scan rates identify good electrochemical double

layer behaviors of the catalysts. While the integrated CV area is proportional to the EDLC and thus surface area, it was found that the ECT-X-CoO showed a higher surface area than that of the pristine CoO at the same scan rate of 10 mV s⁻¹ (Figure

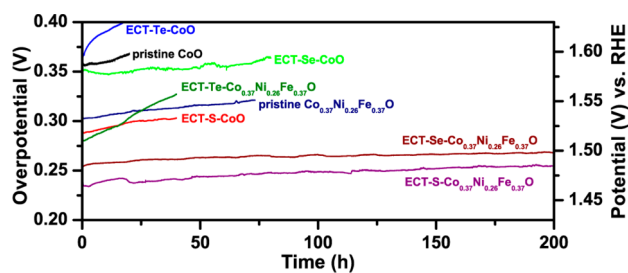


Figure 6. Long-term electrolysis behaviors of the ECT-X-TMOs and the pristine TMOs at a current density of 20 mA cm^{-2} in 1 M KOH.

S13a). Specifically, their surface areas are in the order of $\text{ECT-S-CoO} > \text{ECT-Se-CoO} > \text{ECT-Te-CoO} > \text{pristine CoO}$. In terms of EDLC, the ECT-S-CoO and ECT-Se-CoO exhibit high areal capacitances of 270 and 121 mF cm^{-2} , respectively, superior to that of the pristine CoO with an areal capacitance of 41 mF cm^{-2} (Figure S13b). The ECT-Te-CoO showed a slightly higher capacitance (58 mF cm^{-2}) than that of the pristine CoO, but lower than their S and Se derivatives. The enhanced surface area of the chalcogenides derived oxides and their significantly enhanced OER activities over the pristine oxides is a direct indicator of the successful in situ electrochemical oxidation tuning that was applied to the MXs. It was well-known that the metal species are regarded as the active sites for water oxidation.^{65,66} The enhancement of the OER performance of our catalysts is a result of synergistic effects by the in situ electrochemical tuning. On the one hand, the increase of the electroactive surface area is a strong evidence of the increase of exposed electroactive site, as was observed by some previous studies.^{15,67} Considering that the number of the metal species is not changed for the pristine and the electrochemically derived metal oxides, the derived nanoporous metal oxides have more exposed surface sites than that of the pristine ones. On the other hand, the electrochemical tuning has created a significant amount of defects on the metal oxides, which can provide as extra electroactive sites to further catalyze water oxidation.^{59,68} Moreover, the increased oxidation states of metal species may contribute partially to the enhanced water oxidation.^{63,69} However, it is hard to identify the nature and to quantify the number of the electroactive sites in our electrocatalysts.

On the basis of the different characterizations of the ECT-X-TMOs compared to the pristine TMOs, we have observed significant materials evolution and the correlated catalytic activity enhancement induced by in situ electrochemical oxidation tuning. In order to mimic the electrochemical tuning process for a better understanding of the catalysts structure–property correlations, we illustrate the catalyst’s in situ evolution by taking the binary CoSe_2 with the stable (100) plane as an example (Figure S14). During the in situ electrochemical oxidation process, the CoSe_2 are directly contacted with the strong alkaline solution of KOH, where the amount of OH^- ions is significantly higher than that of the Se_2^{2-} . Over the anodic scan of the catalysts, the OH^- ions migrate to the surface of the Se–Co–Se and react with the catalysts by attacking their Se–Co–Se bonds. The Se–Co–Se bonds start to become weak under the applied external current or voltage. With the increased currents pass through the CoSe_2 catalyst, the Se–Co–Se bonds are broken due to the replacement of –Se groups by –OH groups. In the meanwhile, the positive charged cobalt atoms are tend to interact with the

negative charged OH^- groups to form cobalt oxide or hydroxide. As a result, the CoSe_2 are easily oxidized in the KOH electrolyte under applied anodic scans. Considering the large number of OH^- over the Se_2^{2-} , the CoSe_2 catalysts become highly active to be fully oxidized within even one consecutive scan, which is confirmed by the CV behaviors of CoSe_2 (Figure 1f). In terms of the electrochemical activity of the chalcogens in the order of $\text{S} > \text{Se} > \text{Te}$, the in situ oxidation intensity of the MXs are displayed as $\text{MS}_2 > \text{MSe}_2 > \text{MTe}_2$ as shown in Figure 1e–g and Figure S9. The displacement of the chalcogens with the hydroxide ions results in significant crystal detachment, orientation, atomic diffusion, and recrystallization, therefore offering great opportunities to tune the property of the catalysts. In the meantime, owing to the small radius of hydroxide ions compared to the chalcogens, a tremendous amount of small nanocrystals with tiny grain boundaries and nanopores among them can be generated accordingly, tuning the catalysts to smaller sizes with much enhanced surface area and active sites. The experimental observation and schematic illustration reveal that, although the MXs are fundamentally not stable in alkaline medium during electrochemical measurements, they can be employed as excellent WOC candidates to derive nanoporous TMOs by the facile in situ electrochemical oxidation tuning.

In summary, we have systematically demonstrated in this study that a whole family of transition metal chalcogenides derived nanoporous oxides as excellent water oxidation catalysts. The transformation of the chalcogenides into oxides was achieved by a facile in situ electrochemical oxidation tuning approach and further visualized by different characterization tools, revealing their significant materials evolution and the correlated water oxidation activity. The greatly enhanced oxygen evolution activities of the metal chalcogenides derived nanoporous oxides were proven as a result of the enhanced surface area and more exposed electroactive sites. This study may shed light on exploiting different transition metal chalcogenides, phosphides, nitrides, and carbides as promising catalysts to oxidize water.

■ ASSOCIATED CONTENT

📄 Supporting Information

The Supporting Information is available free of charge on the ACS Publications website at DOI: [10.1021/acs.nanolett.6b03458](https://doi.org/10.1021/acs.nanolett.6b03458).

Experimental details, additional characterization, OER measurements, and supporting tables (PDF)

■ AUTHOR INFORMATION

Corresponding Author

*E-mail: yicui@stanford.edu.

ORCID

Wei Chen: [0000-0001-7701-1363](https://orcid.org/0000-0001-7701-1363)

Notes

The authors declare no competing financial interest.

■ ACKNOWLEDGMENTS

This work was initiated by the support of the Department of Energy, Office of Basic Energy Sciences, Materials Sciences and Engineering Division, under Contract DE-AC02-76-SFO0515. We acknowledge the support from Global Climate and Energy Projects (GCEP) at Stanford University.

REFERENCES

- (1) Walter, M. G.; Warren, E. L.; McKone, J. R.; Boettcher, S. W.; Mi, Q. X.; Santori, E. A.; Lewis, N. S. *Chem. Rev.* **2010**, *110* (11), 6446–6473.
- (2) Gray, H. B. *Nat. Chem.* **2009**, *1* (1), 7–7.
- (3) Gratzel, M. *Nature* **2001**, *414* (6861), 338–344.
- (4) Cheng, F. Y.; Chen, J. *Chem. Soc. Rev.* **2012**, *41* (6), 2172–2192.
- (5) Steele, B. C. H.; Heinzl, A. *Nature* **2001**, *414* (6861), 345–352.
- (6) McEvoy, J. P.; Brudvig, G. W. *Chem. Rev.* **2006**, *106* (11), 4455–4483.
- (7) Umena, Y.; Kawakami, K.; Shen, J. R.; Kamiya, N. *Nature* **2011**, *473* (7345), 55–65.
- (8) Kanan, M. W.; Nocera, D. G. *Science* **2008**, *321* (5892), 1072–1075.
- (9) Ruttinger, W.; Dismukes, G. C. *Chem. Rev.* **1997**, *97* (1), 1–24.
- (10) Yagi, M.; Kaneko, M. *Chem. Rev.* **2001**, *101* (1), 21–35.
- (11) Dau, H.; Limberg, C.; Reier, T.; Risch, M.; Roggan, S.; Strasser, P. *ChemCatChem* **2010**, *2* (7), 724–761.
- (12) Subbaraman, R.; Tripkovic, D.; Chang, K. C.; Strmcnik, D.; Paulikas, A. P.; Hirunsit, P.; Chan, M.; Greeley, J.; Stamenkovic, V.; Markovic, N. M. *Nat. Mater.* **2012**, *11* (6), 550–557.
- (13) McCrory, C. C. L.; Jung, S. H.; Peters, J. C.; Jaramillo, T. F. *J. Am. Chem. Soc.* **2013**, *135* (45), 16977–16987.
- (14) Concepcion, J. J.; Jurss, J. W.; Brenneman, M. K.; Hoertz, P. G.; Patrocino, A. O. T.; Iha, N. Y. M.; Templeton, J. L.; Meyer, T. J. *Acc. Chem. Res.* **2009**, *42* (12), 1954–1965.
- (15) Xu, K.; Chen, P. Z.; Li, X. L.; Tong, Y.; Ding, H.; Wu, X. J.; Chu, W. S.; Peng, Z. M.; Wu, C. Z.; Xie, Y. *J. Am. Chem. Soc.* **2015**, *137* (12), 4119–4125.
- (16) Liang, H. F.; Meng, F.; Caban-Acevedo, M.; Li, L. S.; Forticaux, A.; Xiu, L. C.; Wang, Z. C.; Jin, S. *Nano Lett.* **2015**, *15* (2), 1421–1427.
- (17) Song, F.; Hu, X. L. *Nat. Commun.* **2014**, *5*, 4477.
- (18) Tuysuz, H.; Hwang, Y. J.; Khan, S. B.; Asiri, A. M.; Yang, P. D. *Nano Res.* **2013**, *6* (1), 47–54.
- (19) Yang, Y.; Fei, H. L.; Ruan, G. D.; Xiang, C. S.; Tour, J. M. *ACS Nano* **2014**, *8* (9), 9518–9523.
- (20) Li, H.; Wu, J. M. T.; Yin, Z. Y.; Zhang, H. *Acc. Chem. Res.* **2014**, *47* (4), 1067–1075.
- (21) Tan, C. L.; Zhang, H. *Chem. Soc. Rev.* **2015**, *44* (9), 2713–2731.
- (22) Zhang, H. *ACS Nano* **2015**, *9* (10), 9451–9469.
- (23) Wang, H. T.; Yuan, H. T.; Hong, S. S.; Li, Y. B.; Cui, Y. *Chem. Soc. Rev.* **2015**, *44* (9), 2664–2680.
- (24) Yuan, H. T.; Wang, H. T.; Cui, Y. *Acc. Chem. Res.* **2015**, *48* (1), 81–90.
- (25) Wang, Q. H.; Kalantar-Zadeh, K.; Kis, A.; Coleman, J. N.; Strano, M. S. *Nat. Nanotechnol.* **2012**, *7* (11), 699–712.
- (26) Xu, M. S.; Liang, T.; Shi, M. M.; Chen, H. Z. *Chem. Rev.* **2013**, *113* (5), 3766–3798.
- (27) Wang, H.; Yu, L. L.; Lee, Y. H.; Shi, Y. M.; Hsu, A.; Chin, M. L.; Li, L. J.; Dubey, M.; Kong, J.; Palacios, T. *Nano Lett.* **2012**, *12* (9), 4674–4680.
- (28) Kong, D. S.; Wang, H. T.; Cha, J. J.; Pasta, M.; Koski, K. J.; Yao, J.; Cui, Y. *Nano Lett.* **2013**, *13* (3), 1341–1347.
- (29) Morosan, E.; Zandbergen, H. W.; Dennis, B. S.; Bos, J. W. G.; Onose, Y.; Klimczuk, T.; Ramirez, A. P.; Ong, N. P.; Cava, R. J. *Nat. Phys.* **2006**, *2* (8), 544–550.
- (30) Laursen, A. B.; Kegnaes, S.; Dahl, S.; Chorkendorff, I. *Energy Environ. Sci.* **2012**, *5* (2), 5577–5591.
- (31) Yun, W. S.; Han, S. W.; Hong, S. C.; Kim, I. G.; Lee, J. D. *Phys. Rev. B: Condens. Matter Mater. Phys.* **2012**, *85* (3), 033305.
- (32) Jariwala, D.; Sangwan, V. K.; Lauhon, L. J.; Marks, T. J.; Hersam, M. C. *ACS Nano* **2014**, *8* (2), 1102–1120.
- (33) Voiry, D.; Salehi, M.; Silva, R.; Fujita, T.; Chen, M. W.; Asefa, T.; Shenoy, V. B.; Eda, G.; Chhowalla, M. *Nano Lett.* **2013**, *13* (12), 6222–6227.
- (34) Podzorov, V.; Gershenson, M. E.; Kloc, C.; Zeis, R.; Bucher, E. *Appl. Phys. Lett.* **2004**, *84* (17), 3301–3303.
- (35) Stephenson, T.; Li, Z.; Olsen, B.; Mitlin, D. *Energy Environ. Sci.* **2014**, *7* (1), 209–231.
- (36) Komsa, H. P.; Kotakoski, J.; Kurasch, S.; Lehtinen, O.; Kaiser, U.; Krashennikov, A. V. *Phys. Rev. Lett.* **2012**, *109* (3), 035503.
- (37) Kong, D. S.; Cha, J. J.; Wang, H. T.; Lee, H. R.; Cui, Y. *Energy Environ. Sci.* **2013**, *6* (12), 3553–3558.
- (38) Lu, Q. P.; Yu, Y. F.; Ma, Q. L.; Chen, B.; Zhang, H. *Adv. Mater.* **2016**, *28* (10), 1917–1933.
- (39) Li, Y. G.; Wang, H. L.; Xie, L. M.; Liang, Y. Y.; Hong, G. S.; Dai, H. J. *J. Am. Chem. Soc.* **2011**, *133* (19), 7296–7299.
- (40) Xie, J. F.; Zhang, J. J.; Li, S.; Grote, F.; Zhang, X. D.; Zhang, H.; Wang, R. X.; Lei, Y.; Pan, B. C.; Xie, Y. *J. Am. Chem. Soc.* **2013**, *135* (47), 17881–17888.
- (41) Pumera, M.; Sofer, Z.; Ambrosi, A. *J. Mater. Chem. A* **2014**, *2* (24), 8981–8987.
- (42) Yang, J.; Shin, H. S. *J. Mater. Chem. A* **2014**, *2* (17), 5979–5985.
- (43) Kong, D. S.; Wang, H. T.; Lu, Z. Y.; Cui, Y. *J. Am. Chem. Soc.* **2014**, *136* (13), 4897–4900.
- (44) Zhang, X.; Lai, Z. C.; Tan, C. L.; Zhang, H. *Angew. Chem., Int. Ed.* **2016**, *55* (31), 8816–8838.
- (45) Zhao, W. W.; Zhang, C.; Geng, F. Y.; Zhuo, S. F.; Zhang, B. *ACS Nano* **2014**, *8* (10), 10909–10919.
- (46) Zhou, W. J.; Wu, X. J.; Cao, X. H.; Huang, X.; Tan, C. L.; Tian, J.; Liu, H.; Wang, J. Y.; Zhang, H. *Energy Environ. Sci.* **2013**, *6* (10), 2921–2924.
- (47) Liu, Q.; Jin, J. T.; Zhang, J. Y. *ACS Appl. Mater. Interfaces* **2013**, *5* (11), 5002–5008.
- (48) Gao, M. R.; Xu, Y. F.; Jiang, J.; Zheng, Y. R.; Yu, S. H. *J. Am. Chem. Soc.* **2012**, *134* (6), 2930–2933.
- (49) Liu, Y.; Cheng, H.; Lyu, M.; Fan, S.; Liu, Q.; Zhang, W.; Zhi, Y.; Wang, C.; Xiao, C.; Wei, S.; Ye, B.; Xie, Y. *J. Am. Chem. Soc.* **2014**, *136* (44), 15670–15675.
- (50) Gao, M. R.; Cao, X.; Gao, Q.; Xu, Y. F.; Zheng, Y. R.; Jiang, J.; Yu, S. H. *ACS Nano* **2014**, *8* (4), 3970–3978.
- (51) Tang, C.; Cheng, N. Y.; Pu, Z. H.; Xing, W.; Sun, X. P. *Angew. Chem., Int. Ed.* **2015**, *54* (32), 9351–9355.
- (52) Chen, W.; Wang, H.; Li, Y.; Liu, Y.; Sun, J.; Lee, S.; Lee, J.-S.; Cui, Y. *ACS Cent. Sci.* **2015**, *1* (5), 244–251.
- (53) Caban-Acevedo, M.; Faber, M. S.; Tan, Y. Z.; Hamers, R. J.; Jin, S. *Nano Lett.* **2012**, *12* (4), 1977–1982.
- (54) Feng, Y. J.; He, T.; Alonso-Vante, N. *Electrochim. Acta* **2009**, *54* (22), 5252–5256.
- (55) Sun, R. S.; Chan, M. K. Y.; Ceder, G. *Phys. Rev. B: Condens. Matter Mater. Phys.* **2011**, *83* (23), 235311.
- (56) Chao, Y. S.; Tsai, D. S.; Wu, A. P.; Tseng, L. W.; Huang, Y. S. *Int. J. Hydrogen Energy* **2013**, *38* (14), 5655–5664.
- (57) Yang, J.; Cheng, G. H.; Zeng, J. H.; Yu, S. H.; Liu, X. M.; Qian, Y. T. *Chem. Mater.* **2001**, *13* (3), 848–853.
- (58) Vanderheide, H.; Hemmel, R.; Vanbruggen, C. F. *J. Solid State Chem.* **1980**, *33* (1), 17–25.
- (59) Liu, Y. W.; Cheng, H.; Lyu, M. J.; Fan, S. J.; Liu, Q. H.; Zhang, W. S.; Zhi, Y. D.; Wang, C. M.; Xiao, C.; Wei, S. Q.; Ye, B. J.; Xie, Y. *J. Am. Chem. Soc.* **2014**, *136* (44), 15670–15675.
- (60) Gao, M. R.; Liu, S. A.; Jiang, J.; Cui, C. H.; Yao, W. T.; Yu, S. H. *J. Mater. Chem.* **2010**, *20* (42), 9355–9361.
- (61) Yang, J.; Liu, H. W.; Martens, W. N.; Frost, R. L. *J. Phys. Chem. C* **2010**, *114* (1), 111–119.
- (62) Schenck, C. V.; Dillard, J. G.; Murray, J. W. *J. Colloid Interface Sci.* **1983**, *95* (2), 398–409.
- (63) McAlpin, J. G.; Surendranath, Y.; Dinca, M.; Stich, T. A.; Stoian, S. A.; Casey, W. H.; Nocera, D. G.; Britt, R. D. *J. Am. Chem. Soc.* **2010**, *132* (20), 6882–6883.
- (64) Zheng, Y. R.; Gao, M. R.; Gao, Q.; Li, H. H.; Xu, J.; Wu, Z. Y.; Yu, S. H. *Small* **2015**, *11* (2), 182–188.
- (65) Hamdani, M.; Singh, R. N.; Chartier, P. *Int. J. Electrochem. Sc.* **2010**, *5* (4), 556–577.
- (66) Burke, M. S.; Kast, M. G.; Trotochaud, L.; Smith, A. M.; Boettcher, S. W. *J. Am. Chem. Soc.* **2015**, *137* (10), 3638–3648.

- (67) Kibsgaard, J.; Chen, Z. B.; Reinecke, B. N.; Jaramillo, T. F. *Nat. Mater.* **2012**, *11* (11), 963–969.
- (68) Diaz-Morales, O.; Ledezma-Yanez, I.; Koper, M. T. M.; Calle-Vallejo, F. *ACS Catal.* **2015**, *5* (9), 5380–5387.
- (69) Plaisance, C. P.; van Santen, R. A. *J. Am. Chem. Soc.* **2015**, *137* (46), 14660–14672.